Journal of Power Sources 196 (2011) 6070–6078

Contents lists available at ScienceDirect

Journal of Power Sources

journal homepage: www.elsevier.com/locate/jpowsour

The impact of etching during microfabrication on the microstructure and the electrical conductivity of gadolinia-doped ceria thin films

Anja Bieberle-Hütter*, Patrick Reinhard, Jennifer L.M. Rupp, Ludwig J. Gauckler

Nonmetallic Inorganic Materials, ETH Zurich, Wolfgang-Pauli-Str. 10, HCI G539, CH-8093 Zurich, Switzerland

ARTICLE INFO

Article history:
Received 10 January 2011
Received in revised form 28 February 2011
Accepted 27 March 2011
Available online 4 April 2011

Keywords:
Solid oxide fuel cell
Thin films
Microstructures
Microfabrication
Etching
Conductivity

ABSTRACT

Gadolinia-doped ceria, $Ce_{0.8}Gd_{0.2}O_{1.9-x}$ (CGO), thin films deposited by spray pyrolysis and annealed to different degree of crystallinity between 0% and 95% are exposed to different etchants and etching methods. The attack of the etchants on the CGO thin films is analyzed with respect to changes in microstructure and in-plane electrical conductivity. It is found that amorphous CGO films are dissolved in hydrochloric acid after elongated etching times. Hydrofluoric acid severely attacks CGO thin films after already short times of exposure (1 min), more intense the less crystalline the thin film is. Ar ion etching smoothens the surface of the CGO thin films without considerable removal of material. No microstructural attack of NaOH, CHF_3/O_2 and SF_6/Ar is found. The electrical conductivity is in general only affected when microstructural changes are severe. Therefore, it is concluded that CGO thin films can be well used as functional layers in micro-fabricated devices and that micro-fabrication is, with the exception of hydrofluoric, not harmful for the electrical properties of crystalline CGO thin films.

© 2011 Elsevier B.V. All rights reserved.

1. Introduction

Gadolinia-doped ceria (CGO) is a mixed ionic – electronic conductor with high ionic conductivity at rather low temperatures [1,2]. It is therefore a very promising material for solid oxide fuel cell (SOFC) applications. In particular, micro-SOFC systems [3–6] require high ionic conducting electrolytes at low temperatures in order to qualify for battery replacement in portable equipment, such as laptops, digital assistants, medical or industrial devices. The heart of these micro-SOFC systems is the micro-SOFC membrane. A review about micro-SOFC membrane designs illustrates that most micro-SOFC membranes are fabricated by thin film deposition and etching of adjacent material [7]. The performance of the membranes is, however, mostly very low when compared to thick film systems [7]. This can be due to processing related failures such as cracks and pinholes, but also to the fact that the properties of thin films are often different from bulk material due to strain [8,9], degree of crystallinity [10–12], porosity, very small grain size [13–17]. The influence of microfabrication on the properties of ionic conducting electrolyte thin films was not investigated in detail so far and it is not known whether the performance of functional thin films is affected by etching processes of adjacent layers during microfabrication. In particular, halogen elements such as F^- or Cl^- ions could diffuse into the functional layers and could degrade the electrical conductivity.

Fig. 1 shows a schematic cross section of a typical micro-SOFC multi-layer membrane on a substrate. The arrows indicate the locations where material was etched in order to fabricate either the free-standing membrane (bottom arrows) (refer e.g. to [18–27]) or the microstructured well-defined electrode (top arrows) (refer e.g. to [28–36]). The CGO electrolyte is the adjacent layer here for both etching steps and is therefore shortly exposed to etchant when the etchant approaches the interface in the end of the etching process. In order not to attack the CGO thin film, a selective etchant is chosen which easily attacks the sacrifice material. Table 1 summarizes the current literature on the fabrication of free-standing membranes and micro-patterned electrodes by etching [18,19,26,28,32,35–37]. Wet and dry etching methods are used; dry etching is usually carried out in a reactive ion etching device either in the chemical way using reactive gases (RIE_c) or physically by Ar for example (RIE_p). The etchant is specific to the material that has to be etched. Etching times for the sacrifice material are usually between 5 min and 30 min which signifies that the functional material is only shortly exposed to etchant.

CGO is well known to be very resistant to most etchants and etching methods. Studies investigating the etching of ceria based materials found that mainly chlorine and fluorine plasmas are able to remove ceria based materials with etching rates between 0.0002 and 0.03 $\mu m\ min^{-1}$ depending on the processing and etching method [38–40]. Recently, a first study on the impact of thin film microstructure on the etching characteristics of hydrofluoric acid (HF) was published for CGO thin films prepared by spray pyrolysis [41]. It was found that the microstructure, in specific the degree of crystallinity of the thin CGO films, determines its stabil-

* Corresponding author. Tel.: +41 44 633 6826; fax: +41 44 632 1132.
E-mail address: anja.bieberle@alumni.ethz.ch (A. Bieberle-Hütter).

0378-7753/$ – see front matter © 2011 Elsevier B.V. All rights reserved.
doi:10.1016/j.jpowsour.2011.03.082

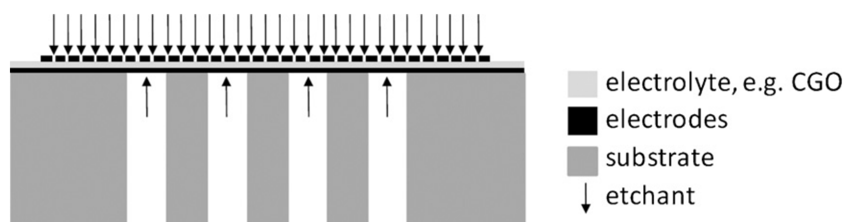

Fig. 1. Schematic cross section of free-standing micro-SOFC membranes; arrows indicate were etchant gets in contact with functional layers.

ity towards HF. An amorphous thin film is already attacked by 10% HF:H_2O after 1 min of exposure. Fully crystalline thin films are less attacked by HF than partially crystalline and amorphous films. An overview of etching rates of bulk and thin film CGO under different wet or dry etching methods is given in [41]. No information is available on the impact of the etching on the electrical properties of CGO which is of major interest in view of microfabrication of micro-SOFC membranes with CGO electrolytes.

In this study, we therefore investigate the impact of wet and dry etchants, which are typically used in microfabrication of micro-SOFC membranes or micro-patterned electrodes, on the microstructure and the electrical properties of CGO thin films deposited by spray pyrolysis. The CGO thin films were post-annealed at different temperatures and had therefore different degree of crystallinity.

2. Experimental

2.1. Thin film deposition

Gadolinia-doped ceria ($Ce_{0.8}Gd_{0.2}O_{1.9-x}$, CGO) thin films were deposited by spray pyrolysis on sapphire substrates (∅ = 3.5 cm) from Stettler, Switzerland. The substrates were covered with a stainless steel mask during deposition having an open window of 1.4 cm × 2.5 cm.

Appropriate amounts of cerium nitrate ($Ce(NO_3)_3{\cdot}6H_2O$, Merck) and gadolinium chloride ($GdCl_3{\cdot}6H_2O$, Alfa Aesar) were dissolved in a tetraethylene glycol (TEG, 99% purity, Aldrich) and water solution (ratio 9:1) in order to obtain a 0.1 M metallic salts precursor solution.

Spray pyrolysis was carried out by an air blast atomizer from a distance of 39 cm at a substrate temperature of 390 ± 5 °C measured on the substrate surface with a contact thermometer. All samples were sprayed for 60 min at a spray rate of 5 ml h^{-1} and air pressure of 1 bar. Light microscopy (Polyvar-MET) was used to check the quality of the as-deposited amorphous thin films.

2.2. Thermal treatment

Some thin films were heat treated to transform the originally amorphous films into the partially or fully crystalline state. Heat treatment was carried out in air in a Nabertherm (Controller P320, Nabertherm, Switzerland) furnace with a heating and cooling rate of 3 °C min^{-1}. Thin films annealed at 600 °C for 10 min are partially crystalline with about 30% crystallinity. Thin films annealed at 1000 °C for 10 min are almost fully crystallized with about 95% crystallinity. The degree of crystallinity was adjusted with the annealing temperature and time as reported earlier in [10] for identically processed CGO thin films.

2.3. Etching

Samples of all degree of crystallinity were etched for different times by wet and dry etching. The etching times were selected considering typical etching times which are used in the literature for fabricating free-standing membranes and micro-patterned electrodes according to Table 1. However, it has to be noted that the CGO functional layers themselves are in these applications much shorter exposed to etchant; in fact, the CGO is only exposed to the etchant when the interface between adjacent layer and CGO is reached. Hence, exposure times in reality are much shorter than the etching times used in this study.

2.3.1. Wet etching

Hydrochloric acid (HCl), sodium hydroxide (NaOH), and hydrofluoric acid (HF) of different concentrations (see Table 2) were used as wet chemical etchants for 1, 10 or 60 min under constant stirring. After the completion of the etching step, the samples were thoroughly washed with de-ionized water in order to remove and neutralize all the acid. Detailed etching parameters are given in Table 2.

2.3.2. Dry etching

Dry etching was carried out in a RIE 80 Insulator (Oxford Instruments RIE 80+) using CHF_3/O_2 and SF_6/Ar (later called as “chemical reactive ion etching” (RIE_c)) and in a RIE 76 (Oxford Instruments Plasmalab 80) using Ar (later called as “physical reactive ion etching” (RIE_p)). Detailed etching parameters are given in Table 2.

2.4. Microstructural characterization

Microstructure and film thicknesses were investigated with scanning electron microscope (SEM, LEO 1530, Germany). Top view and cross section images were taken from all samples using an EHT

Table 1
Overview on etching methods and etchants used for the fabrication of freestanding membranes and micro-patterned electrodes.

Etching method	Etchant	Etched material	Purpose	Etching time in Ref. [min]	Ref.
Wet etching	HCl	Perovskites	Patterned electrode	10–20	[28,35]
	NaOH	Metal alloys	3D structured electrode	10	[36]
	HF	Foturan	Free-standing membrane	30	[18]
	EDP[a]	Si	Free-standing membrane	NA	[37]
Dry etching					
Chemically (RIE_c)	CHF_3/O_2	Si_xN_y	Free-standing membrane	5–7	[26,27]
	SF_6/O_2	Si_xN_y	Free-standing membrane	NA	[19]
Physically (RIE_p)	Ar	Perovskites	Free-standing membrane	<140	[32]

[a] Ethylenediamine-pyrocatechol.

Table 2
Etching parameter used in this study.

Etching method	Etchant	Etching conditions	Etching time [min]
Wet etching	HCl	37% fuming, RT[a]	10, 60
	NaOH	14% aqueous (4M), RT[a]	1, 10
Dry etching	HF	10% aqueous, RT	1, 10
Chemically (RIE_c)	CHF_3/O_2	50 sccm/50 sccm, 50 mTorr, 20 °C, 150 W	5, 10
	SF_6/O_2	15 sccm/15 sccm, 50 mTorr, 20 °C, 50 W	5, 10
Physically (RIE_p)	Ar	100 mbar, 10 °C, 200 W	20, 60

[a] Room temperature.

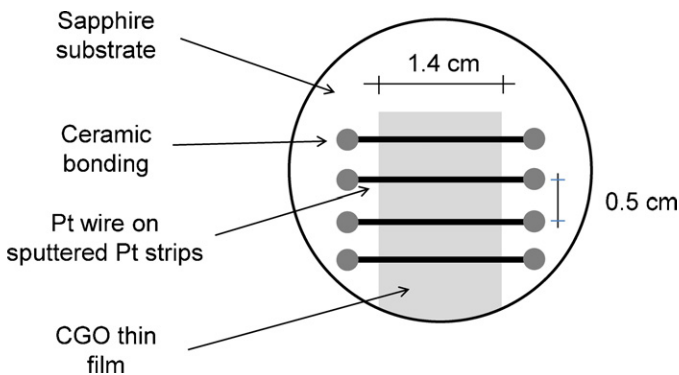

Fig. 2. Schematic representation of the thin film sample for conductivity measurement.

beam of 3 kV and after coating the surfaces with a 4-5 nm thick platinum film. Cross section images were obtained by carefully breaking the sapphires after inducing a crack on the back side of the sapphire single crystal with a diamond pen. The thicknesses of the thin films were measured from SEM cross sections after electrical measurement. The presented values were averaged out of 10 random measurements at different locations of the sample with a magnification of 50,000×. The error in film thickness is in average about 14%.

2.5. Conductivity measurements

Electrical resistance of the CGO thin films was measured as a function of temperature by 4-point conductivity method. Four platinum electrodes were sputtered onto the thin films with a BALTEC SCD 050 sputter-ion pump for 5 min at a current of 60 mA resulting in about 100 nm thick Pt electrodes. A stainless steel mask was used to obtain 4 narrow contact strips with 5 mm distance between them as shown in Fig. 2. Platinum wires (thermocouple quality, 0.127 mm diameter, 5 cm length, JM Noble metals) were flattened under a hydraulic press and glued on the sputtered Pt-film with a Pt-conducting paste (C 3605 S, HERAEUS) and a two-component ceramic glue on the outside of the film. The contacted films were put into a drying oven at 120 °C for 20 min to cure the ceramic glue.

The Pt-electrode wires were connected to a Keithley 2700 Multimeter/Data acquisition system (Keithley, Germany) and the resistance of the thin films was measured in a tube furnace (Lenton, England) with simultaneous, in situ temperature measurement. The resistance of the thin films was recorded as a function of temperature by LabView (Version 8.5, Texas Instruments). In order to avoid microstructural changes during conductivity measurements, the highest temperatures for the resistance measurement were set 100 °C and 50 °C lower than the maximum annealing temperature for fully and partially crystalline samples, respectively. Measurements were carried out for 2 cycles between 300 °C and the highest allowed temperature (depending on the crystallinity of the sample) with a heating and cooling rate of 3 °C min^{-1} and dwell time of 1 h. Resistance measured in the first cooling cycle was used for calculation of the conductivity.

An overview on the thermal and processing history of the thin films as well as the degree of crystallinity is given in Table 3. Amorphous thin films (A_{etched}) are etched directly after thin film deposition, but were not subjected to any thermal treatment after deposition. The highest temperatures these films have seen are the deposition temperature. A_{etched}/PC30 thin films are etched directly after deposition and are not annealed. However, they crystallized in situ during electrical conductivity measurement up to about 580 °C and are therefore 30% crystalline according to [10] after electrical conductivity measurement. $PC30_{etched}$ and $FC95_{etched}$ thin films were annealed for 10 min to 600 °C and 1000 °C, respectively. These films were etched after annealing and were electrically characterized up to 580 °C and 900 °C, respectively. They are about 30% and 95% crystalline [10].

The error in conductivity data was estimated to be mainly due to the error in the measurements of thin film thicknesses and thickness variations of the thin films. The error bars in the conductivity data are based on this estimation.

3. Results and discussion

3.1. Microstructure

Fig. 3 shows typical top and cross section SEM images of CGO thin films that were subjected to different thermal treatment in the non-etched state. The thermal histories and the degree of crystallinity of these thin films are summarized in Table 3. In Fig. 3a and b, an as-deposited, amorphous (A) thin film is shown. Fig. 3c and d picture an 30% crystalline thin film; the same microstructures are found after deposition and subsequent electrical conductivity measurement up to 580 °C (A/PC30) and for thin films that were post-annealed at 600 °C for 10 min and electrically characterized up to 580 °C (PC30). Fig. 3e and f illustrate an 95% crystalline thin film after post-annealing at 1000 °C for 10 min and electrical con-

Table 3
Thermal and processing history and degree of crystallinity of the CGO thin films in this study.

Sample ID	Annealing		Time of etching	T_{max} during electrical conductivity	Degree of crystallinity according to [10]
	T_{max}	t			
A_{etched}	NA	NA	After deposition	NA	Amorphous
A_{etched}/PC30	NA	NA	After deposition	580 °C	Amorphous/30%
$PC30_{etched}$	600 °C	10 min	After annealing	580 °C	30%
$FC95_{etched}$	1000 °C	10 min	After annealing	900 °C	95%

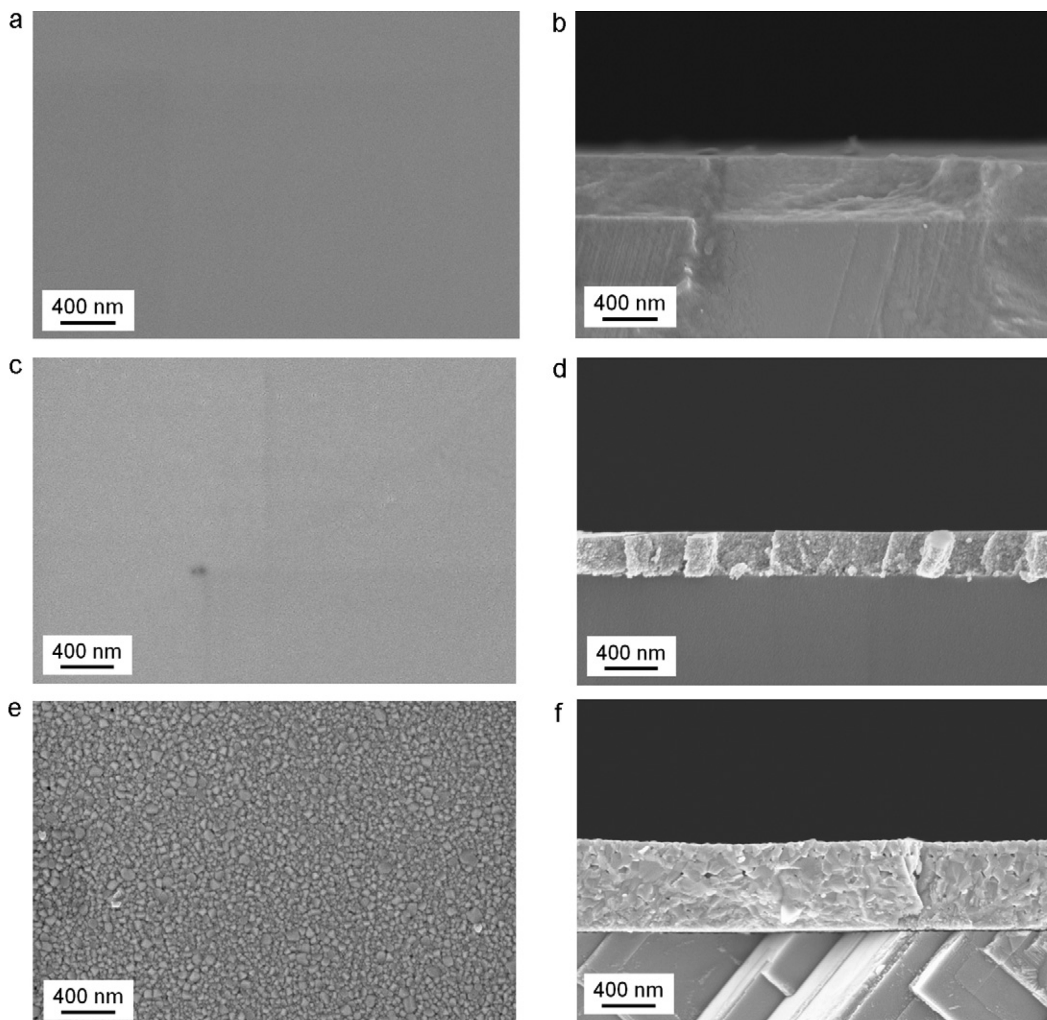

Fig. 3. SEM top and cross section micrographs of CGO thin films without etching: (a–b) amorphous, as-deposited (A), (c–d) 30% crystalline (A/PC30, PC30), (e–f) 95% crystalline (FC95). For the thermal history and the degree of crystallinity of all samples refer to Table 3 and the explanations in the experimental part.

ductivity measurement up to 900 °C (FC95). The microstructures of PC30 and FC95 thin films, respectively, were the same after merely annealing and after annealing plus electrical conductivity measurement; hence, stable microstructures were obtained after annealing for 10 min dwell time.

All films are very homogeneous and dense from the top view (Fig. 3a, c, e). The as-deposited, amorphous (Fig. 3a) and the partially crystalline thin films (Fig. 3c) are very smooth with no surface structure or roughness visible by SEM. In the top view image of the 95% crystalline thin film, distinct grains with grain sizes smaller than 100 nm and thermally etched grain boundaries are visible (Fig. 3e).

Cross section micrographs show good adhesion of all films to the sapphire substrate. Besides the amorphous thin film (Fig. 3b), all thin films have a granular structure after thermal treatment which is typical for thin films deposited by spray pyrolysis (Fig. 3d, f). Grains are much larger and more distinct for the 95% crystalline thin film (Fig. 3f) compared to the 30% crystalline samples (Fig. 3d). The 95% crystalline microstructure (Fig. 3f) shows pores. These pores were confirmed by focused ion beam analysis and are therefore intrinsic to the structure and not related to grain pull out due to sample preparation by breaking for SEM analysis.

The effect of etching on the microstructures depends strongly on the kind of etchant, the etching time, and the degree of crystallinity of the thin films. No changes of the microstructures were found after etching with RIE_c with CHF_3/O_2 and SF_6/Ar for 10 min as well as with 10 min NaOH solution according to SEM analysis. HCl, HF, and RIE_p (Ar), in contrast, attacked the microstructures as described in the following.

Fig. 4 shows top view images of as-deposited, amorphous CGO thin film after exposure to HCl. After 10 min of etching, small holes are seen in the thin film which signify small attack of the HCl towards the CGO thin film (Fig. 4a). Fig. 4b shows a sample that was partly protected during HCl etching. After 60 min of HCl etching, the unprotected film (left side) is dissolved from the substrate, while the protected film (right side) is only partly attacked. Note that this long etching time of 60 min is a much exaggerated time scale, since adjacent layers such as CGO are usually only shortly exposed to the etchant even much shorter than typical etching times as listed in Table 1. 30% and 95% crystalline CGO thin films are not attacked by HCl even for very long and exaggerated exposure to the etchant.

Fig. 5 shows top view images of CGO thin films after HF etching. Comparing these images to the non-etched top views in Fig. 3, it can be seen that the partially crystalline thin films with 30% crystallinity (Fig. 5a and b, respectively) are significantly attacked after 1 min HF etching. The microstructures are riddled with lengthy holes and the structure is not connected at the surface anymore. The fully crystalline thin film in contrast (Fig. 5c) is not attacked after 1 min HF etching. However, after 10 min HF exposure (Fig. 5d), round pores are visible at grain triple points. In agreement with [41], we see that the grain boundaries are preferably etched. Hence, the microstruc-

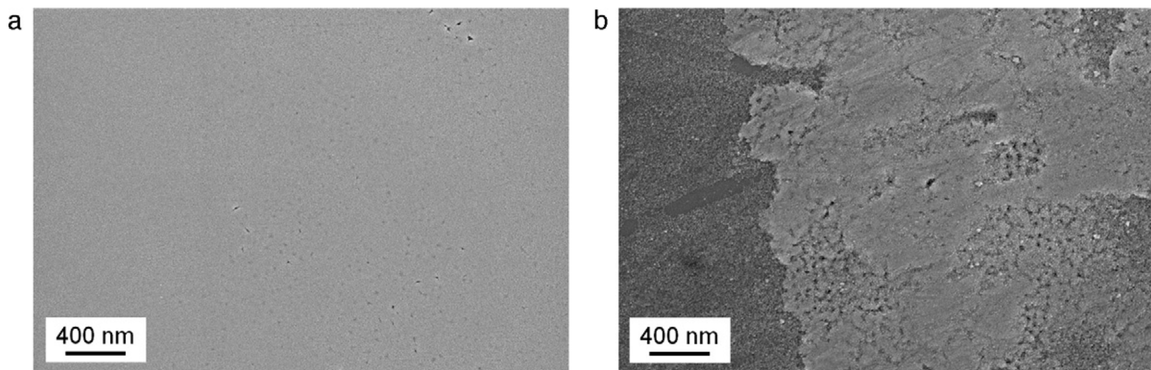

Fig. 4. Top view image of as-deposited, amorphous CGO thin film after HCl etching: (a) 10 min, (b) 60 min: left part was fully exposed to HCl and the entire film is dissolved; right part was protected and is only partially dissolved.

tures of CGO thin films are significantly attacked by HF etching already after rather short etching times. These observations are in agreement with [41].

Fig. 6 shows top view images of 95% crystalline CGO thin films after RIE_p treatment. Compared to Fig. 3, one finds small pores after 20 min exposure to RIE_p as well as a smoothening of the grains. After long RIE_p treatment the grains cannot be distinguished anymore and the surface of the sample is fully flattened. Similar microstructural changes are found for amorphous and partially crystalline thin films.

In summary, it was found that the microstructures of CGO thin films are stable with respect to RIE_c (CHF_3/O_2 and SF_6/Ar for 10 min) and to 10 min NaOH etching. HCl attacks amorphous CGO thin films, but does not attack thin films annealed to 30% or 95% crystallinity. Films are heavily attacked by HF after already rather short etching times. RIE_p (Ar) etching smoothens the surface of the thin films.

3.2. *Thin film thickness*

The thicknesses of the thin films were determined after etching and conductivity measurement and are plotted together with the standard deviations in Fig. 7. Usually the data for the samples with the longest etching times are plotted because they pose the most severe conditions on the thin films and material removal is supposed to be detected best. Mainly for HF etching, the 1 min data is plotted, since microstructure analysis already revealed that the thin films are severely attacked after 1 min of etching; hence, it is of main interest whether 1 min etching already reduces the film thickness significantly.

The thicknesses of the 30% crystalline (A_{etched}/PC30 and $PC30_{etched}$) and the 95% crystalline ($FC95_{etched}$) thin films before etching are rather similar with an average thickness of 386 ± 70 nm. This error in film thickness is typical for thin films deposited by

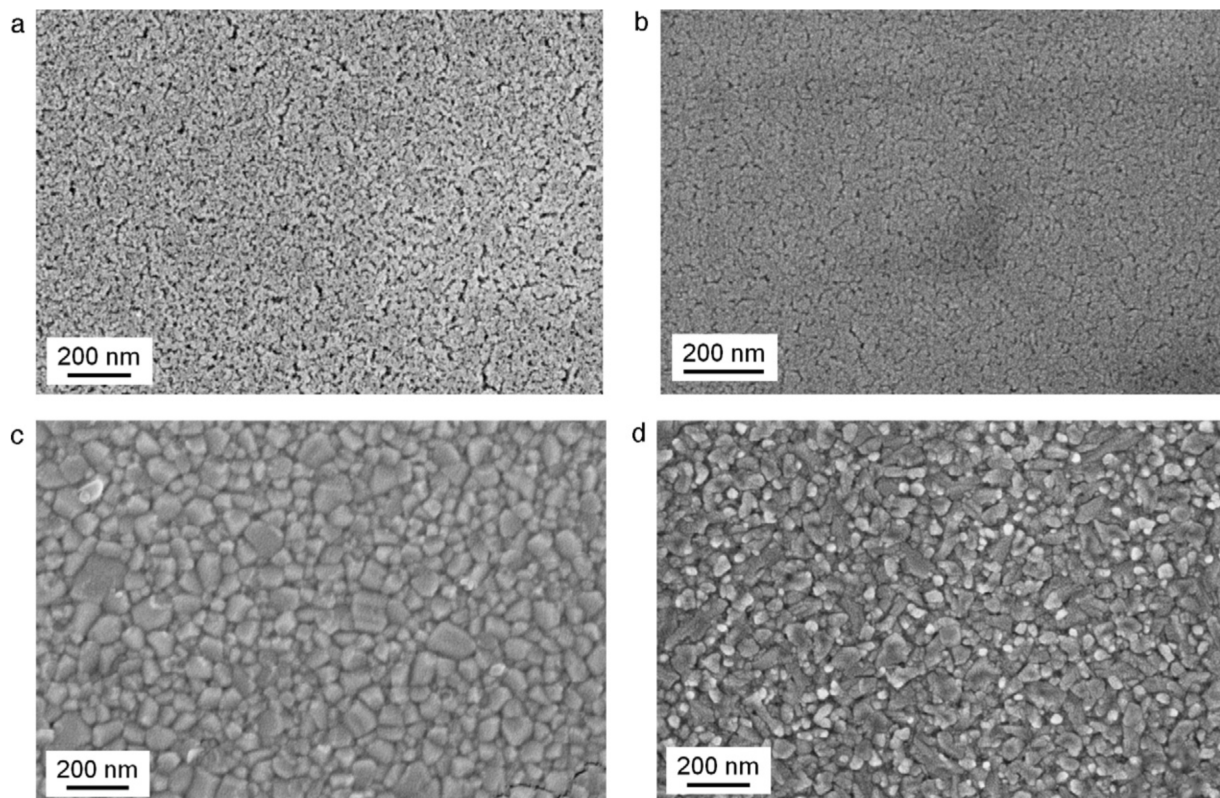

Fig. 5. Top view images of CGO thin films after HF etching: (a) 30% crystalline thin film (A_{etched}/PC30) after 1 min HF, (b) 30% crystalline thin film ($PC30_{etched}$) after 1 min HF, (c) 95% crystalline thin film ($FC95_{etched}$) after 1 min HF, (d) 95% crystalline thin film ($FC95_{etched}$) after 10 min HF.

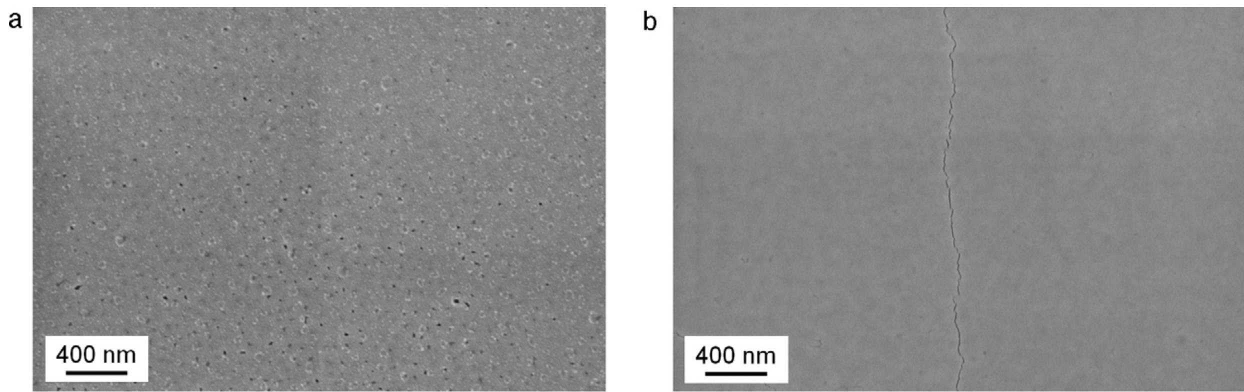

Fig. 6. Top view images of 95% crystalline CGO thin films after RIE_p etching: (a) 20 min and (b) 60 min.

spray pyrolysis deposition. It signifies that most volume change due to shrinkage of the thin films during thermal annealing takes place up to a temperature of 600 °C.

The film thicknesses of the etched films are almost all in the error range of the non-etched films for all degree of crystallinity. Hence, no considerable material removal took place for most etchants. The only exception is the 30% crystalline thin film A_{etched}/PC30 which was etched by HCl for 60 min. This thin film is considerably attacked by HCl exposure and the thickness is strongly decreased. This is clear since the A_{etched}/PC30 thin films are etched directly after deposition in the amorphous state and get partially crystalline due to in situ annealing during electrical conductivity measurement. Hence, the degraded microstructure is inherited from low etching resistance of the amorphous thin film. The observations are in agreement with the microstructure findings in Fig. 4. Please note that HF etching of 1 min and 10 min as well as RIE_p etching did not reduce the thickness of the thin films according to Fig. 7. Hence, the microstructural changes in Figs. 5 and 6, respectively, are restricted to the surface and material is not considerably removed.

3.3. Electrical conductivity

Conductivity data for non-etched CGO thin films are shown in Fig. 8 for different degree of crystallinity. For the non-annealed thin film, both the heating and the cooling curves are shown. The heating curve represents the first thermal treatment of the amorphous thin film, while the cooling curve considers the thermal treatment during conductivity measurement. Due to this in situ annealing, the thin film is about 30% crystalline (A/PC30) after the first cycle of electrical conductivity measurement [10]. For all degrees of crystallinity, the conductivity increases with increasing temperature. The as-deposited, thin film (open squares) has the lowest conductivity of all films and the highest activation energy (E_A = 2.25 eV) which is related to the amorphous state and the high amount of precursor residues that remained still in the thin film which both hinder ion diffusion. The corresponding cooling curve (A/PC30 with closed squares) shows slightly higher conductivity at the same maximum temperature due to a short isothermal dwell before cooling and related crystallization of the thin film. The conductivities of the partial crystalline thin films, A/PC30 and PC30, are rather similar. Both thin films have about the same degree of crystallinity. The small differences in the conductivity can be attributed to the different thermal history with longer time at high temperature in the case of PC30. The 95% crystalline thin film has the highest conductivity with an activation energy of 0.93 eV similar to data published earlier [42]. The small discontinuity around 650 °C is an artifact due to the measurement device during changing the measuring range. It

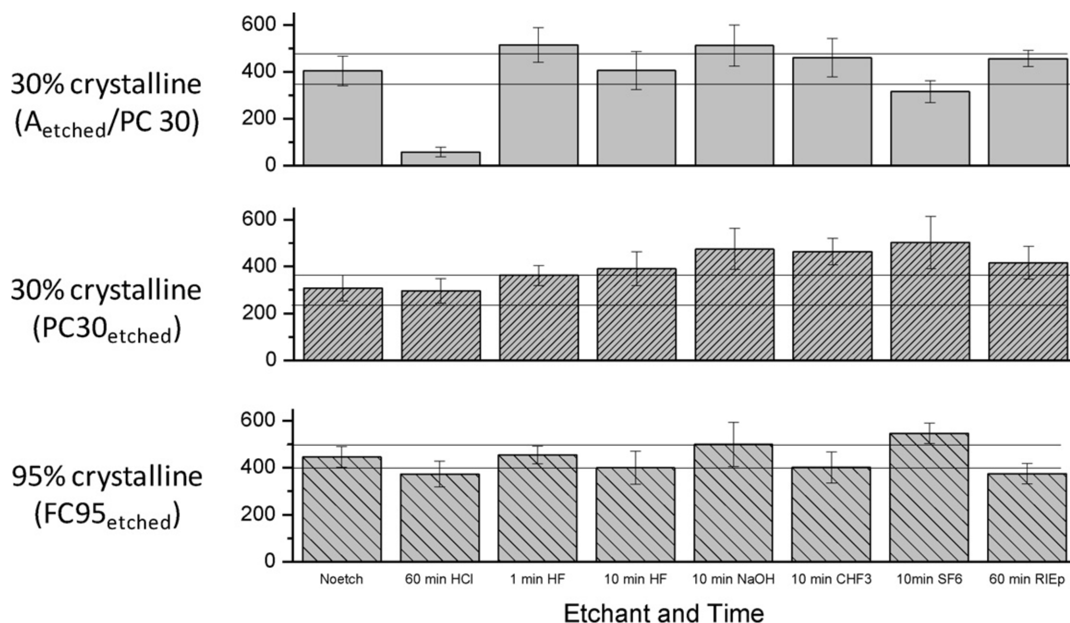

Fig. 7. Thicknesses of partially and fully crystalline CGO thin films after electrical conductivity measurements derived from SEM cross section images. The error in film thickness is determined from 10 measurements on one sample.

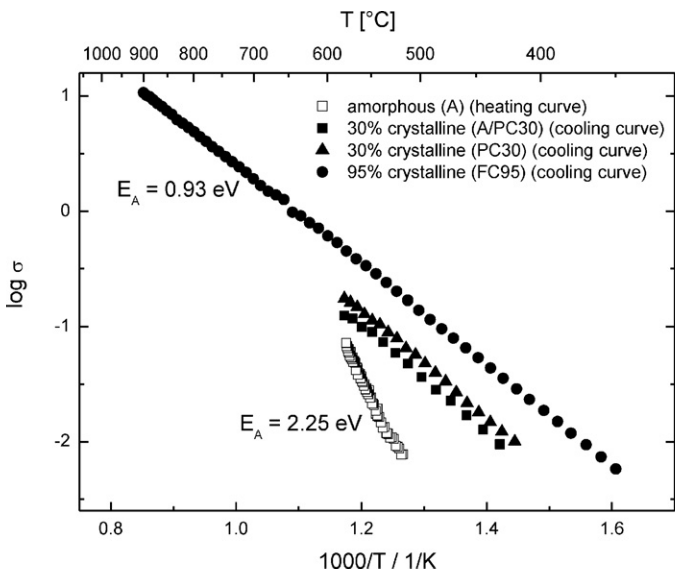

Fig. 8. Conductivity as a function of temperature for non-etched CGO thin films for different degree of crystallinity; open symbols: first heating curve; closed symbols: first cooling curve. Please note that the activation energy was determined from the ln(σT) vs. 1000/T plot. Error bars have similar size as the symbols and are therefore not shown.

has no significant effect on the conductivity data or the activation energy.

The conductivity of the non-etched samples (Fig. 8) is compared to samples that were etched prior to electrical conductivity measurement in Fig. 9. Generally, the data for the longest etching times used in this study are shown. The heating curves of the as-deposited, amorphous thin films are shown in Fig. 9a. The conductivity increases with increasing temperature, similarly like for the non-etched sample. RIE etching (CHF_3/O_2, SF_6, Ar) as well as wet etching with NaOH does not impact the conductivity considering the error in conductivity measurement of about 14% due to the uncertainty in the thickness of the thin films. However, relatively short etching of HCl for 10 min as well as HF for 1 min decreased the conductivity slightly. The sample that was etched for 1 min in HF shows the largest activation energy which might be attributed to the effect of surface adsorbents from the etching process. Longer etching with HF up to 10 min decreased the conductivity even more. This is in perfect agreement with the microstructure analysis where considerable attack of amorphous thin films by HCl and HF was found (Figs. 4 and 5, respectively). The discontinuities of the conductivity data at high temperatures are related to the sintering of the contacting paste. Strong discontinuities are measured between 550 and 650 °C also for fully crystalline sample during the first heating. These discontinuities vanish after annealing at temperatures higher than 650 °C. Fig. 9b and signify the 30% crystalline thin film due to in situ crystallization during the heating cycle of the electrical conductivity measurement. All data is within half an order

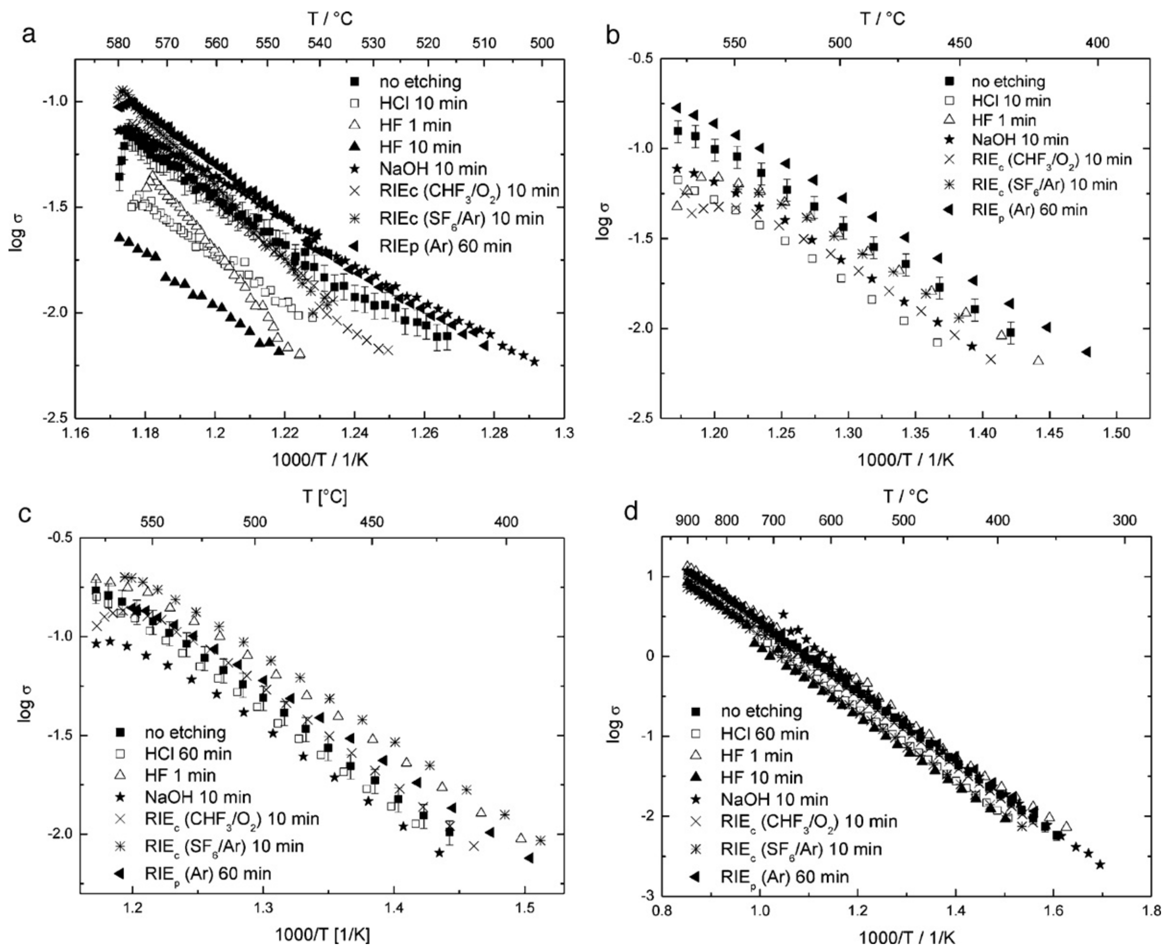

Fig. 9. Conductivity as a function of temperature for different etchants, different degree of crystallinity and time of etching: (a) amorphous (A_{etched}) (heating curve), (b) 30% crystalline after in situ crystallization (A_{etched}/PC30) (cooling curve), (c) 30% crystalline after annealing ($PC30_{etched}$) (cooling curve), (d) 95% crystalline after annealing ($FC95_{etched}$) (cooling curve). Error bars refer to an accuracy of about 14% of the conductivity measurements mainly due to the error in the measurements of thin film thicknesses and thickness variations of the films.

Table 4
Summary of impact of etching on CGO thin films deposited by spray pyrolysis. Abbreviations A, A/PC30, PC30, FC95 according to Table 3; check mark means "no attack" and cross means "attack" of CGO thin film by etchant.

	Wet etching											
Etchant	HCl				HF				NaOH			
t_{max}	10 min/60 min				1 min/10 min				10 min			
Degree of crystallinity	A	A/PC30	PC30	FC95	A	A/PC30	PC30	FC95	A	A/PC30	PC30	FC95
Microstructure	×/×	×/×	√/√	√/√	×/×	×/×	×/×	√/×	√	√	√	√
Thickness	√/×	√/×	√/√	√/√	√/√	√/√	√/√	√/√	√	√	√	√
Electrical conductivity	√/×	√/×	√/√	√/√	√/×	√/×	√/×	√/√	√	√	√	√

	RIE_c								RIE_p			
Etchant	CHF_3/O_2				SF_6/Ar				Ar			
t_{max}	10 min				10 min				60 min			
Degree of crystallinity	A	A/PC30	PC30	FC95	A	A/PC30	PC30	FC95	A	A/PC30	PC30	FC95
Microstructure	√	√	√	√	√	√	√	√	×	×	×	×
Thickness	√	√	√	√	√	√	√	√	√	√	√	√
Electrical conductivity	√	√	√	√	√	√	√	√	√	√	√	√

of magnitude which means that no significant difference in the conductivity is found between non-etched and etched thin films. Even the shortly etched HCl and the HF etched film do not show a decrease in conductivity or changed activation energy as found in the heating curves of the amorphous thin film (Fig. 9a). Hence, the observed effects in the heating data in Fig. 9a are not significant and might be related to surface adsorbents after the etching process. This also means that the conductivity is stable, even though the microstructure is already attacked by the etchant in the case of 1 min HF and 10 min HCl.

The conductivities of 30% crystalline thin films which were etched after post-deposition annealing at 600 °C are shown in Fig. 9c. The conductivities scatter within half an order of magnitude. Considering the error in film thickness determination, it can be concluded that no considerable impact of any etchants on the conductivity of 30% crystalline thin films was found for the considered etching times.

The conductivities of the 95% crystalline CGO thin films are shown in Fig. 9d. Scattering in the conductivity data of half an order of magnitude is found for the different thin films. The discontinuities of the conductivity data of the 60 min HCl, the 10 min SF_6/Ar, and the 10 min HF thin films around 750 °C are related to the measurement set up. Considering the scattering in the determination of the film thickness, it can be concluded that no significant impact of etching on the conductivities was found.

4. Summary and conclusions

The impact of etching during microfabrication of free-standing membranes and electrodes on the microstructure and the electrical conductivity of gadolinia doped ceria (CGO) functional thin films was investigated. CGO thin films with different degree of crystallinity were exposed to different etching methods, etchants and etching times. The overall results are summarized in Table 4 where check marks mean "no attack" and crosses signify that the thin film was damaged and the properties, i.e. microstructure, film thickness or electrical conductivity, were changed. No impact of etching on microstructure and electrical conductivity was found for the wet etchant NaOH and for reactive ion etching with CHF_3/O_2 and SF_6/Ar. Ar reactive ion etching smoothens the topography after long etching times without considerable material removal and no impact on the conductivity. Wet chemical etching with HF is most critical from all etchants and etching methods investigated in this study.

HF attacks the microstructure of CGO thin films (the less crystalline the thin film, the more the microstructure is attacked) as well as the electrical conductivity. However, it was found that the electrical conductivity does not degrade after short etching times of 1 min, even though microstructural changes are already visible. Fully crystalline films are stable in conductivity up to 10 min HF etching.

Hydrochloric acid attacks amorphous CGO thin films both in microstructure and in electrical conductivity after very long and exaggerated etching of 60 min. No significant impact on the conductivity of partially and fully crystalline thin films was found.

In view of processing of microfabricated solid state ionic devices, we conclude that

(1) Solid state ionic functional thin films are very robust towards etching and can be well combined with microfabrication without negative impact on the conduction properties of the thin films. No evidence for detrimental diffusion of etchant into functional layers is found.
(2) The degree of crystallinity of thin films is of main importance concerning the robustness of thin films towards etching and microfabrication in general. The more crystalline a film is the more stable it is.
(3) Microstructural analysis by SEM is sensitive to detect possible impact of etchants on the thin films and their properties. In this study, electrical conductivity was only affected when microstructural impact was already detected. Hence, small microstructural damage does not degrade the electrical conductivity.

Acknowledgments

The SOFC group at Nonmetallic Inorganic Materials at ETH Zurich is thanked for experimental support; in particular A. Evans, T. Ryll, and R. Tölke are thanked for assistance in etching.

Financial assistance by the following Swiss institutions is gratefully acknowledged: Center of Competence Energy and Mobility (CCEM) within the framework of the ONEBAT Project; Competence Center for Materials Science and Technology (CCMX) within the framework of the NANCER Project; Swiss Electric Research (SER) within the framework of the ONEBAT Project; and Swiss National Foundation (SNF) within the framework of the Sinergia Project ONEBAT.

References

[1] M. Mogensen, N.M. Sammes, G.A. Tompsett, Solid State Ionics 129 (2000) 63–94.
[2] B.C.H. Steele, Solid State Ionics 129 (2000) 95–110.
[3] A. Bieberle-Hütter, D. Beckel, A. Infortuna, U.P. Muecke, J.L.M. Rupp, L.J. Gauckler, S. Rey-Mermet, P. Muralt, N.R. Bieri, N. Hotz, M.J. Stutz, D. Poulikakos, P. Heeb, P. Müller, A. Bernard, R. Gmür, T. Hocker, J. Power Sources 177 (2008) 123–130.
[4] D. Nikbin, The Fuel Cell Review (April/May 2006) 21–24.
[5] S.B. Schaevitz, A. Franz, R. Barton, W, A.P. Ludwiszewski, in, USA, 2006.
[6] G.J. LaO, H.J. In, E. Crumlin, G. Barbastathis, Y. Shao-Horn, Int. J. Energy Res. 31 (2007) 548–575.
[7] A. Evans, A. Bieberle-Hütter, J.L.M. Rupp, L. Gauckler, J. Power Sources 194 (2009) 119–129.
[8] A. Kushima, B. Yildiz, J. Mater. Chem. (2010) 4809–4819.
[9] J.L.M. Rupp, A. Infortuna, L.J. Gauckler, Acta Materialia 54 (7) (2006) 1721–1730.
[10] J.L.M. Rupp, B. Scherrer, N. Schäuble, L.J. Gauckler, Adv. Funct. Mater. 20 (2010) 2807–2814.
[11] J.L.M. Rupp, C. Solenthaler, P. Gasser, U.P. Muecke, L.J. Gauckler, Acta Mater. 55 (2007) 3505–3512.
[12] J.L.M. Rupp, B. Scherrer, L.J. Gauckler, Phys. Chem. Chem. Phys. 12 (2010) 11114–11124.
[13] N.I. Karageorgakis, A. Heel, J.L.M. Rupp, M. Aguirre, T. Graule, L.J. Gauckler, Adv. Funct. Mater. 21 (3) (2010) 532.
[14] I. Kosacki, T. Suzuki, V. Petrovsky, H.U. Anderson, Solid State Ionics 136 (2000) 1225–1233.
[15] T. Suzuki, I. Kosacki, H.U. Anderson, Solid State Ionics 151 (2002) 111–121.
[16] W.C. Jung, J. Hertz, H. Tuller, Acta Mater. 57 (2009), 1399-1304.
[17] B. Butz, H. Störmer, D. Gerthsen, M. Bockmeyer, R. Krüger, E. Ivers-Tiffee, M. Luysberg, J. Am. Ceram. Soc. 91 (2008) 2281–2289.
[18] U.P. Muecke, D. Beckel, A. Bieberle-Hütter, S. Graf, A. Infortuna, J.L.M. Rupp, J. Schneider, L.J. Gauckler, Adv. Funct. Mater. 18 (2008) 1–11.
[19] P. Su, C. Chao, J. Shim, R. Fasching, F. Prinz, Nano Lett. 8 (2008) 2289–2292.
[20] J.H. Shim, C. Chao, H. Huang, F.B. Prinz, Chem. Mater. 15 (2007) 3850–3854.
[21] H. Huang, M. Nakamura, P. Su, R. Fasching, Y. Saito, F.B. Prinz, J. Electrochem. Soc. 154 (2007) B20–B24.
[22] S. Rey-Mermet, P. Muralt, Solid State Ionics 179 (2008) 1497–1500.
[23] I. Garbayo, A. Tarancon, J. Santiso, F. Peiro, E. Alarcon-Lado, A. Cavallaro, I. Garcia, C. Cane, N. Sabate, Solid State Ionics 181 (2010) 322–331.
[24] A. Tarancon, N. Sabate, A. Cavallaro, I. Gracia, J. Roqueta, I. Garbayo, J.P. Esquivel, G. Garcia, C. Cane, J. Santiso, J. Nanosci. Nanotechnol. 10 (2010)1327–1337.
[25] A.C. Johnson, A. Baclig, D.V. Harburg, B. Lai, S. Ramanathan, J. Power Sources 195 (2010) 1149–1155.
[26] R. Tölke, private communication.
[27] C. Gatzert, A.W. Blakers, P.N.K. Deenapanray, J. Vac. Sci. Technol. A 24 (2006) 1857–1865.
[28] A. Bieberle-Hutter, H.L. Tuller, J. Electroceram. 16 (2006) 151–157.
[29] V. Brichzin, J. Fleig, H.U. Habermeier, G. Cristiani, J. Maier, Solid State Ionics 152 (2002) 499–507.
[30] J. Fleig, F.S. Baumann, V. Brichzin, H.R. Kim, J. Jamnik, G. Cristiani, H.U. Habermeier, J. Maier, Fuel Cells 6 (2006) 284–292.
[31] E. Koep, C. Compsona, M. Liua, Z. Zhoub, Solid State Ionics 176 (2005) 1.
[32] T. Ryll, J.L.M. Rupp, A. Bieberle-Hütter, H. Galinski, L.J. Gauckler, Scripta Mater., in press, doi:10.1016/j.scriptamat.2010.09.022.
[33] T. Horita, K. Yamaji, N. Sakai, X.P. Xiong, T. Kato, H. Yokokawa, T. Kawada, J. Power Sources 106 (2002) 224–230.
[34] A. Bieberle, L.P. Meier, L.J. Gauckler, J. Electrochem. Soc. 148 (2001) A646–A656.
[35] N.J. Simrick, J.A. Kilner, A. Atkinson, J.L.M. Rupp, T.M. Ryll, A. Bieberle-Hütter, H. Galinski, L.J. Gauckler, Solid State Ionics, in press, doi:10.1016/j.ssi.2010.03.025.
[36] T. Ryll, PhD Thesis, ETH Zurich, Switzerland, 2011.
[37] Bruschi, Thin Solid Films 346 (1999) 151–254.
[38] A. Kossoy, M. Greenberg, K. Gartsman, I. Lubomirsky, J. Electrochem. Soc. 152 (2005) C65–C66.
[39] C.-S. Oh, C.-I. Kim, K.H. Kwon, J. Vac. Sci. Technol. A 19 (2001) 1068–1071.
[40] S. Shim, Y.S. Kwon, S.I. Kim, Y.T. Kima, J.H. Park, J. Vac. Sci. Technol. A 22 (2004) 1559–1563.
[41] J.L.M. Rupp, U.P. Muecke, P.C. Nalam, L.J. Gauckler, J. Power Sources 195 (2010) 2669–2676.
[42] J.L.M. Rupp, L.J. Gauckler, Solid State Ionics 177 (2006) 2513–2518.